Microfluidics and the Observation of Fluid Flow Through Four Different Channels

Sara Parvaresh Rizi | AER210 | November 12, 2025

1. Introduction

Microfluidics is the study of systems with fluids inside channels of microscopic widths. Microfluidic devices have been used to detect cancers, analyze DNA, and study bacteria, among other applications [1].

The objective of this experiment is to validate theoretical microfluidic flow models by measuring bead velocities in channels of varying geometry. An important equation for incompressible flow of a streamline is Bernoulli's Equation, shown below, for density ρ, speed v, gravity g, height z, and pressure P.

$$\frac{1}{2}\rho v^2 + \rho g z + P = constant \qquad (1)$$

Note that Equation (1) does not apply to viscous and turbulent flow. However, other methods to model these flows are complex, so an ideal laminar flow approximation is used. At steady flow, the volume of fluid past a cross-sectional area is assumed to be constant with respect to time. From conservation of mass, Equation (2) applies, where A_i, v_i refers to the cross-sectional area and speed of fluid at point i, respectively.

$$\int v_1 dA_1 = \int v_2 dA_2 \qquad (2)$$

If the flow is constant in any cross-section, it reduces to the continuity equation $v_1 A_1 = v_2 A_2$. Furthermore, for volume flow rate Q, pressure difference ΔP, dynamic viscosity coefficient μ, and length of pipe section L, Hagen-Poiseuille's law [2] gives Equation (3), for an incompressible, Newtonian fluid in laminar flow through a cylindrical pipe.

$$Q = \frac{S^2}{8\pi\mu L}(\Delta P + \rho g \Delta z) \qquad (3)$$

In this report, I will use the above equations to examine the flow of fluid through four different channels (straight, bent, gradual change, sharp change), and discuss their behaviors in each one.

2. Experimental Procedures

The experiment used a microscope to observe fluid flow through a polydimethylsiloxane (PDMS) microfluidic chip. The chip was connected with tubing to a syringe, mounted on a movable stand to control the driving pressure through a hydrostatic head (syringe height). A reservoir collected the waste fluid. The working fluid was a suspension of fluorescent beads in ethanol. Flow was induced by gravity, and bead motion was captured with the microscope's camera in fluorescence (TX2 filter) mode. Flow velocity (v) was determined by measuring the streak length (d) of beads during a known camera exposure time (t) using the relation $v = \frac{d}{t}$. A detailed step-by-step procedure is provided in the lab manual [2].

To convert from pixels to physical units, the scale bar present in each image was used. Using MS paint, 44.913 µm corresponded to 288 pixels, giving a conversion factor of 0.1559 µm/pixel. All distance measurements in pixels were multiplied by this factor. The software used to get pixel length had an accuracy of 1 pixel.

3. Error Analysis

I first achieved a quantifiable reading error, as many of the streaks were blurry and getting the width of each wasn't the same each time. A standard deviation of the measurement of one point was taken, to be around 1.817 pixels, higher than 1 pixel, which I took as my reading error.

Each picture had an exposure time associated with it, where the error was taken to be the precision of the measurement to the least significant digit (e.g. 0.17392 seconds would have ± 0.00001s). Note that because the time measurements were extremely precise, the errors for velocity were dominated by streak measurements.

For the conversion of each pixel measurement to metres, there was error associated with the scale measure, ΔL, being

0.001 μm from the image accuracy. There was also $\Delta px = 1.817\ pixels$, being my reading error. Therefore, the propagated error ΔP for each pixel conversion P for $L = 44.913$ μm, $px = 288\ pixels$ is given in Equation (4), and calculated to be $\Delta P = 0.001$ μm with the stated values.

$$\Delta P = P * \sqrt{\left(\frac{\Delta L}{L}\right)^2 + \left(\frac{\Delta px}{px}\right)^2} \tag{4}$$

When converting from pixels to meters, x, if $x = P * d$, for P the conversion factor and d the length in pixels, the propagation Δx is given in Equation (5).

$$\Delta x = x * \sqrt{\left(\frac{\Delta P}{P}\right)^2 + \left(\frac{\Delta d}{d}\right)^2} \tag{5}$$

For example, if $d = 15\ pixels$, $x = 2.34$ μm, P is the conversion factor and $\Delta P = 0.001$ μm/px,

$$\Delta x = 2.339\text{μm} * \sqrt{\left(\frac{0.001}{\frac{44.913}{288}}\right)^2 + \left(\frac{1.817}{15}\right)^2}$$
$$= 0.284\text{μm}$$

To calculate the velocity error, I first took the kinematics equation $v = \frac{x}{t}$, for v velocity, x distance and t time.

Differentiating v with respect to x and t, I achieved the expressions in Equation (6).

$$\frac{\partial v}{\partial x} = \frac{1}{t}, \frac{\partial v}{\partial t} = \frac{-x}{t^2} \tag{6}$$

Using the calculus-derived error propagation [3], I rearranged my terms, going through Equations (7-9) to arrive at Equation (10).

$$(\Delta v)^2 = \left(\frac{\partial v}{\partial x}\Delta x\right)^2 + \left(\frac{\partial v}{\partial t}\Delta t\right)^2 \tag{7}$$

$$\left(\frac{\Delta v}{v}\right)^2 = \frac{1}{v^2}\left(\left(\frac{1}{t}\Delta x\right)^2 + \left(\frac{-x}{t^2}\Delta t\right)^2\right) \tag{8}$$

$$\left(\frac{\Delta v}{v}\right)^2 = \left(\frac{\Delta x}{x}\right)^2 + \left(\frac{\Delta t}{t}\right)^2 \tag{9}$$

$$\Delta v = v\sqrt{\left(\frac{\Delta x}{x}\right)^2 + \left(\frac{\Delta t}{t}\right)^2} \tag{10}$$

Equation (10) gives the final velocity error propagation. A sample calculation with this would be to take an exposure time $t = 0.134s$, $\Delta t = 1ms$, a streak length of $x = 2.339$ μm, $\Delta x = 0.284$μm, and a calculated $v = 0.017\ m/s$, from Equation (5), to yield

$$\Delta v = (0.017\frac{m}{s})\sqrt{\left(\frac{0.284}{2.339}\right)^2 + \left(\frac{1 * 10^{-3}s}{0.134s}\right)^2}$$
$$\Delta v \approx 0.002\ m/s$$

Some non-quantifiable errors that appeared in the chip were air bubbles. An example of this is most prominent in the image for sharp width change, in Figure 5. These caused blockages, increasing local flow velocity and pressure drops, and potentially introducing unsteady, turbulent-like flow patterns.

Note that the visual inspection of the channels showed minor wall imperfections, with roughness estimated from pixel variation to be on the order of 1.092 ± 0.001 μm. This was achieved through taking the standard deviation of wall measurements across images and using error propagation stated in Section 3. These imperfections enhance viscous friction near the walls, distorting the velocity profile from its ideal parabolic shape. This increased wall shear stress leads to a higher pressure drop for a given flow rate and can reduce the mean streamwise velocity. While the impact of these imperfections is likely small compared to other errors like air bubbles, they contribute to a systematic deviation from theoretical predictions.

4. Results and Discussion

In the following section, I will describe the behaviour of the flow through each channel type, and how they follow the equations outlined in the introduction of the report.

4.1. Flow Through a Straight Channel

The flow in the straight channel was observed, with the image shown in Figure 1.

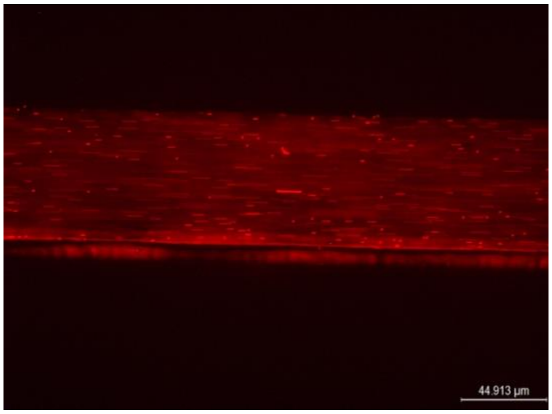

Figure 1 Straight channel image, with scale in the bottom left corner

As seen by the apparently straight flow lines (red streaks), the flow seems to be laminar as no streaks cross each other, and all run parallel to the channel walls.

For pressure-driven laminar flow between two parallel plates, the velocity profile is parabolic, following the no-slip condition. Therefore, the maximum velocity is expected at the channel centerline. Conversely, the maximum velocity gradient (shear rate) occurs at the walls, where the velocity changes from zero to the free-stream value. I observe this trend in Figure 1, where most streaks are shorter near the walls and longer at the center.

The velocity profile of the channel is shown in Figure 2, compared with a parabolic fit in green.

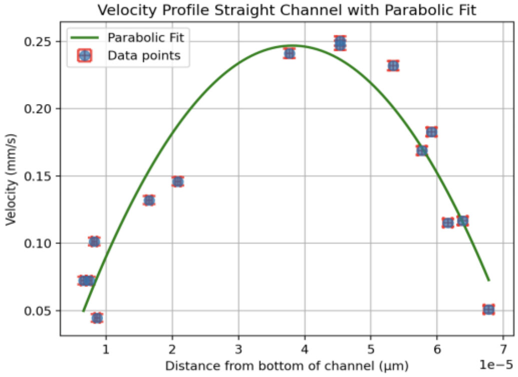

*Figure 2 Velocity profile of the straight channel, with error bars (too small to be seen) and a parabolic fit in green. The equation is v=((1.982±0.211)** 10^{8} *)* x^{2}*+((1.511±17.698)** 10^{4} *)x+(4.126 ±56.67). The R-squared value is around 0.897.*

The measured profile mostly follows a parabolic trend; however, it has high error values for its parameters, meaning it still is not ideal. As well, while the R-squared value is high, it's not very close to 1 (closer to 0.9). This is likely due to the channel imperfections and the difficulty in measuring streaks very close to the center where there is a lot of blur.

Based on the principles behind Bernoulli's equation (Equation (1)), the mean velocity can be manipulated by changing the driving pressure, which is a function of the syringe height (ρgΔz). The experiment was idealized to the model in Figure 3 in the lab manual [2], to derive the relationship between changing channel heights and velocity. For Q the volumetric flow rate, the velocity U past a unit area S would be given by Equation (11).

$$U = SQ \tag{11}$$

From equation 4, $Q = \frac{S^2}{8\pi\mu L}(\Delta P + \rho g \Delta z)$. Between section 1 and 2, and 3 and 4, there is a height difference, therefore both have the form $Q = \frac{S_i^2}{8\pi\mu L_i}(P_i - P_{i+1} + \rho g(z_i - z_{i+1}))$, for i = 1 and 2. For sections 2-3, 3-4, 4-5, 5-6, they are all at the same height, meaning the $\rho g \Delta z$ term cancels, leaving Q= $\frac{S_i^2}{8\pi\mu L_i}(P_i - P_{i+1} + \rho g(z_i - z_{i+1}))$, for i=2,3,4,5. If we were to sum the above, we would get an expression like Equation (12), for $R_j = \frac{8\pi\mu L_j}{S_j^2}$.

$$\sum_i \Delta P_j + \rho g \Delta z_j = Q \sum_i R_j \tag{12}$$

Note that $\sum_i \Delta P_j$ simply equals $P_1 - P_6$, through terms cancelling out, and $\sum_i \rho g \Delta z_j$ equals $\rho g(z_1 - z_3)$. Thus, we arrive at Equation (13).

$$P_1 - P_6 + \rho g(z_1 - z_3) = Q \sum_i R_j \tag{13}$$

If the syringe free surface pressure and exit are both atmospheric, $P_1 - P_6 = 0$, and we get Equation (14).

$$\rho g(z_1 - z_3) = Q \sum_i R_j \tag{14}$$

With Equation (11), $U_3 = S_3 Q$, so we get Equation (15), which can be arranged to Equation (16).

$$\rho g(z_1 - z_3) = \frac{U_3}{S_3} \sum_i R_j \quad (15)$$

$$U_3 = \frac{\rho g(z_1 - z_3)}{S_3 \sum_i R_j} \quad (16)$$

Because all ρ, g, S_3, R_j are constants with known values, we achieve the general formula, Equation (17), where if z_3 is to be taken as a reference height located at $z = 0$, it simplifies to Equation (18).

$$U_3 = k(z_1 - z_3) = k\Delta z \quad (17)$$

$$U_3 = kz_1 \quad (18)$$

Thus, velocity scales linearly with height.

The syringe was changed to four different heights, and the velocity in the channel was measured at the same point at each height. The result of this plotting is shown in Figure 3.

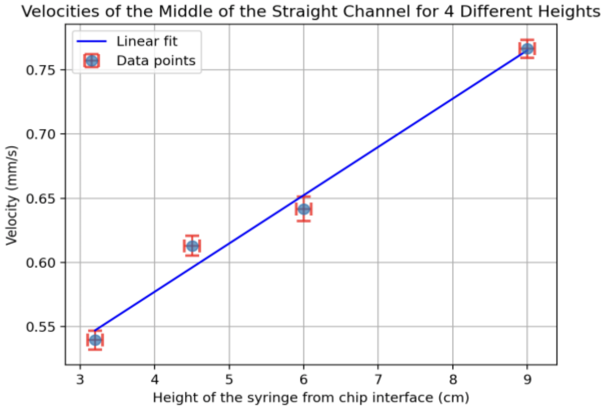

Figure 3 : Changes in velocity within the straight channel at four different heights. The points show a linear trend, approximately following v=(0.037 ± 0.003)x + (0.427±0.008). The R-squared value was around 0.982.

From Figure 3, we see similarities between the linear equation in Equation (18) and the linear trend outlined by the blue line of best fit. The R-squared value is high, close to 1, and the errors are within 1% of values, showing a close relationship between the linear fit and observed data, greatly affirming Equation (18) for change in velocity given different heights. However, the fit is not perfect, likely attributed to errors in height measurement, chip wall imperfections, and reading error.

4.2. Flow Through a Bend

As flow in the chip went through bends, streamlines would crowd together near the outer concave wall, narrowing the stream tube and increasing local velocity, while they expanded near the inner convex corner, contributing to the flow separation. The images for the bent regions are shown in Figure 4.

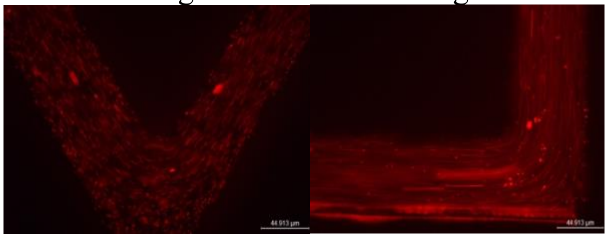

Figure 4 : Images of two bent regions, the right being the smooth (domed) bend and the left the sharp (L-shaped) bend. Most particles are streamlined closer to the middle, and circular eddies form around the bend

Note that in the sharp bend (L-shaped), a prominent flow separation bubble is located at the inner (convex) corner, creating a recirculating eddy. The smooth bend showed a similar, but less prominent separation near the bottom of the U, where most of the streamlines appeared to still be laminar.

This difference arises because the gradual curvature of the smooth bend allows the flow to adhere to the wall, while the abrupt turn in the sharp bend creates an adverse pressure gradient that causes separation. Although the pathlines are curved, they are smooth and do not exhibit the random, chaotic crossing or mixing characteristic of turbulent flow. The observed eddies in the sharp bend are steady, laminar separation bubbles, not turbulent vortices.

The velocities before and after the bend in each type of bend are recorded in Table 1.

Table 1: Velocities recorded before and after bends for both sharp and smooth bends.

Type of Bend	Velocity before bend (mm/s)	Velocity after bend (mm/s)

Sharp (L-shape)	0.726 ± 0.012	0.775 ± 0.012
	0.292 ± 0.011	0.413 ± 0.011
Smooth (domed)	0.212 ± 0.011	0.247 ± 0.011
	0.159 ± 0.006	0.198 ±0.006

For flow through a bend, considering the channel width does not change before and after bends, I originally expected the velocity to decrease because of eddies forming near the curve (where flow would not be streamline). However, the data in Table 1 shows slight increases in velocities before and after bends.

I hypothesize this is due to more complicated theory, such as how flow through a curved pipe develops secondary vortices and the r.m.s. (fluctuation) of velocities increase due to mean strain from curvature [4]. Therefore, the bend introduces a centrifugal force that causes fluid near the outer wall to speed up and a return flow near the inner wall (the 'Dean' vortex pair). The redistribution leads to a higher axial velocity along the centreline (or shifted centre of max velocity) than upstream.

4.3. Effects of Varying Channel Widths

Looking at the channels with width change, the theoretically expected centerline flow velocity ratio was calculated with Equation (19), derived from Equation (3) assuming the height did not change.

$$Q = \frac{S^2}{8\pi\mu L}(\Delta P) \qquad (19)$$

Using the fact that the average flow velocity ($U_{average}$) is half that of the centerline velocity (U_{max}) [2], and conservation of mass, where for volumetric flow rate Q , $Q_{in} = Q_{out}$, we arrive at Equation (20), a restating of Equation (2).

$$S_1 U_{avg,1} = S_2 U_{avg,2} \qquad (20)$$

Relating Equation (20) with $\frac{1}{2}U_{max} = U_{average}$ we get the ratio in Equation (21), for centerline velocities $U_{max,1}$, $U_{max,2}$.

$$\frac{S_1}{S_2} = \frac{U_{max,2}}{U_{max,1}} \qquad (21)$$

Assuming the channels are rectangular, the area ratio would reduce to Equation (22).

$$\frac{S_1}{S_2} = \frac{l * w_1}{l * w_2} = \frac{w_1}{w_2} = \frac{U_{max,2}}{U_{max,1}} \qquad (22)$$

The widths of each channel (gradual and sharp) are recorded in Table 2, for both before and after, noting the ratio change $\frac{S_1}{S_2}$.

Table 2 Widths before and after for gradual and sharp channels, along with the ratio of width before to width after.

Type of channel	Width before (µm)	Width after (µm)	Ratio (before/after)
Gradual	69.017 ±0.686	130.206 ± 1.148	0.530 ± 0.006
Sharp	72.314 ± 0.709	200.254 ± 1.710	0.361 ± 0.010

Note that the error for each ratio was calculated as in Equation (23), for j_1, j_2 quanties before and after, $\Delta\, j$ the error in each quantity, R the ratio and ΔR the error in the ratio. In this case, j_1, j_2 are the widths, $\Delta j_1, \Delta j_2$ the errors in widths, and R the width ratio.

$$\Delta R = R\sqrt{\frac{\Delta j_1}{j_1} + \frac{\Delta j_2}{j_2}} \qquad (23)$$

Similarly, the velocities before and after each channel change were recorded in Table 3, alongside the ratio $\frac{U_{max,2}}{U_{max,1}}$.

Table 3: Velocities before and after for gradual and sharp channels, along with the ratio of velocity after to velocity before.

Type of channel	Velocity before (mm/s)	Velocity after (mm/s)	Ratio (after/before)
Gradual	0.236 ± 0.006	0.112 ± 0.006	0.473±0.028
Sharp	0.538 ± 0.010	0.193 ± 0.009	0.360 ± 0.017

Note that the error propagation for width ratios was used, except for j_1, j_2 and $\Delta j_1, \Delta j_2$ being velocities and error in velocity respectively.

The images for the gradual and sharp transitions are shown in Figure 5. Note that the sharp transition had air bubbles near its corners, which made it more akin to the gradual transition than a sharp width change.

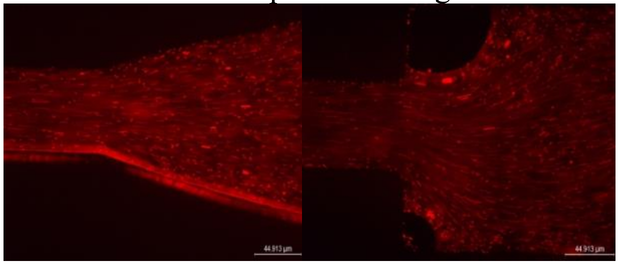

Figure 5 Images of the gradual (left) and sharp (right) channels. The sharp channel has air bubbles in its corners, appearing as dark circles.

The flow remained laminar, as evidenced by the smooth, non-crossing pathlines even after the expansion. The sudden expansion likely resulted in a larger, steady, laminar separation bubble. Because expansion introduces recirculation, local pressure drop increases, slightly reducing measured $U_{max,2}$ relative to theory.

In the gradual transition, the measured ratios were 0.473±0.028, compared to the theoretical of 0.530 ± 0.006, giving around an 11% difference. The reason for this could have stemmed from difficulty measuring the true centerline velocity, slight out-of-plane flow. For the sharp expansion, the measured velocity ratio of 0.360 ± 0.035 showed excellent agreement with the theoretical prediction of 0.361, differing by less than 1%.

Flows are used in everyday lives, such as in home plumbing and HVAC systems, automotive and aerospace engineering, and more. Smooth flow transitions (maintaining laminar flow) are preferred because it results in lower energy consumption, reduced friction and drag, and more predictable, stable flow. Even though in this scenario the sharp transition yielded small error and results closer to theory, this is mostly due to unquantifiable experimental error. Also, it is important to note that the air bubbles in the sharp transition channel mimicked the slow and gradual width change in the gradual change channel, not completely and accurately reproducing behaviour that a regular sharp channel would, which is probably why the results agreed so closely to theory.

5. Conclusion

In summary, the experimental results strongly supported theoretical fluid mechanics principles in a microfluidic context. The relationship between syringe height and channel velocity was confirmed to be linear, as predicted by the viscous-dominated Hagen-Poiseuille model. The principle of mass conservation was validated in width-changing channels, with measured velocity ratios showing excellent agreement (sharp change) and good agreement (gradual change) with theory. While the velocity profile in the straight channel followed a parabolic trend, significant fitting errors highlighted the impact of experimental limitations. The main sources of error were pixel-length measurement uncertainty, channel imperfections, and transient flow effects like air bubbles.

6. References

[1] Tram Anh, “Microfluidics and its applications | Micro Systems,” *Micro Systems - Precision Medical Device Moulding Services*, May 19, 2023. https://www.medicalmoulds.com/microfluidics-and-its-applications/

[2] B. Keith, E. Chung, and T. Dell, “Microfluidics Lab Manual,” 2025.

[3] M. Coombes, “Propagation of Measurement Uncertainties Using Calculus,” *Mikecoombesphysics.ca*, 2025. https://mikecoombesphysics.ca/P1102_Notes/Error_Propagation/Error_Propagation_Calculus.htm (accessed Nov. 11, 2025).

[4] A. K. Vester, “Vortices in turbulent curved pipe flow— rocking, rolling and pulsating motions,” *Technical Reports from Royal Institute of Technology KTH Mechanics*, May 2014, https://www.diva-portal.org/smash/get/diva2%3A717536/FULLTEXT01.pdf?.

7. Appendix

Using Bernoulli's Equation (Equation (1)), if we assume viscous frictional loses are negligible, $S_1 \gg S_i$, and therefore $U_1 \approx 0$ (nozzle approximation). We are also using the same assumption that $P_1 = P_6 = P_{atm}$, and that point 6 is at the reference height so $z_3 = 0$, then Bernouilli's equation reduces to

$$P_{atm} + \frac{1}{2}\rho U_1^2 + \rho g z_1 = P_{atm} + \frac{1}{2}\rho\, U_6^2 + \rho g z_3^2 \tag{1}$$

$$0 + \frac{1}{2}\rho(0)^2 + \rho g z_1 = 0 + \frac{1}{2}\rho\, U_6^2 + (0)^2 \tag{2}$$

$$\rho g z_1 = \frac{1}{2}\rho\, U_6^2 \tag{3}$$

And so, we derive Torricelli's law:

$$U_6 = \sqrt{2gz_1} \tag{4}$$

Using the continuity equation, that

$$Q = S_3 U_3 = S_6 U_6 \tag{5}$$

We can substitute for U_6 and get the relation

$$U_3 = \frac{S_6}{S_3}\sqrt{2gz_1} \tag{6}$$

Considering $S_6, S_3,$ and g are known constants, we can simplify to

$$U_3 = k\sqrt{z_1} \tag{7}$$

For some constant k = $\frac{S_6}{S_3}\sqrt{2g}$. This does not agree with the equation, as it now provides a square root relationship rather than a linear. This is because Hagen-Poiseuille models the microfluidic regime, where flow is dominated by viscous resistance, and the pressure dorp (in turn flow rate) would in turn be linearly proportional to the height different when resistance is constant. This is more accurate to reality, as viscuous forces would dominate over interital forces (giving a low Reynolds number). However, Bernouilli assumes an ideal, inviscid fluid with no energy losses, where the velocity would be related to the conversion of potential energy into kinetic energy.